Heliyon 10 (2024) e23334

Contents lists available at ScienceDirect

Heliyon

journal homepage: www.cell.com/heliyon

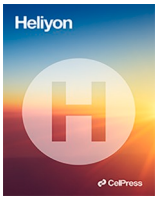

Fuzzy-logic technique for gold mineralization prospecting using Landsat 9 OLI processing and fieldwork data in the Bibemi goldfield, north Cameroon

Safianou Ousmanou [a,b,*], Yaya Fodoue [c], Jacques Wassouo Wadjou [c], Amadou Diguim Kepnamou [d], Eric Martial Fozing [a], Maurice Kwékam [a], Miranda Ikfi [e]

[a] Department of Earth Science, University of Dschang, Dschang, Cameroon
[b] Department of Geological Research, CONGEO-Engineering, Yaounde, Cameroon
[c] Centre for Geological and Mining Research (CRGM), Garoua, Cameroon
[d] Department of Mining Geology, School of Geology and Mining Engineering, University of Ngaoundere, Ngaoundere, Cameroon
[e] National Mining Corporation (SONAMINES), Yaounde, Cameroon

ARTICLE INFO

Keywords:
Gold
Fuzzy
Mineral exploration
Hydrothermal alteration
Bibemi

ABSTRACT

Identifying potential hydrothermal alteration areas is indeed an essential method for mineral exploration. In this research, we developed an algorithm for the delineation of alteration mineral deposits related to gold mineralization in the Bibemi region using set of criteria derived from Landsat 9 OLI data using false colour composites, band ratios, principal component analysis, spectral angle mapper, and fuzzy-logic overlay methods. The methods used showed iron-oxides, ferrous, and hydroxyl-bearing and carbonate mineral properties related to gold mineralization. The fuzzy overlay map identified regions depending on their mineralization prospective, serving as foundation for prospective mineral deposit evaluation investigation, which was produced by the merging of band ratios and PC's alteration markers labelled very good, and excellent and encompasses 0.8–0.9, 0.9–1.0 respectively. The identified regions fit gold mineralization zones based on their potential as proven by prior and field research. In addition, lineaments analysis showed the presence of three main structural direction impacting the Bibemi region (N–S, NNE-SSW, and ESE-WNW to SSE-NNW), when merged with identified rock formations permits the possible deposition of mineral deposits. The innovative aspect of this research is the integration and processing of Landsat 9 OLI and fieldwork data, which allows for the identification of potentially mineralized rock formations and defining exploration targets.

1. Introduction

Satellite imageries could be used to target multiple and new potential areas before conducting detailed and costly fieldwork research [1,6,30,35,50,56,62]. Moreover, the use of satellite data for remote sensing is a crucial low-cost option for detecting, mapping, and gathering dependable information on potential or prospective areas, and actually, enhanced remote sensing data has

* Corresponding author. Department of Earth Science, University of Dschang, Dschang, Cameroon.
E-mail address: safianouousmanou.79@gmail.com (S. Ousmanou).

https://doi.org/10.1016/j.heliyon.2023.e23334
Received 11 July 2023; Received in revised form 30 November 2023; Accepted 30 November 2023
Available online 6 December 2023

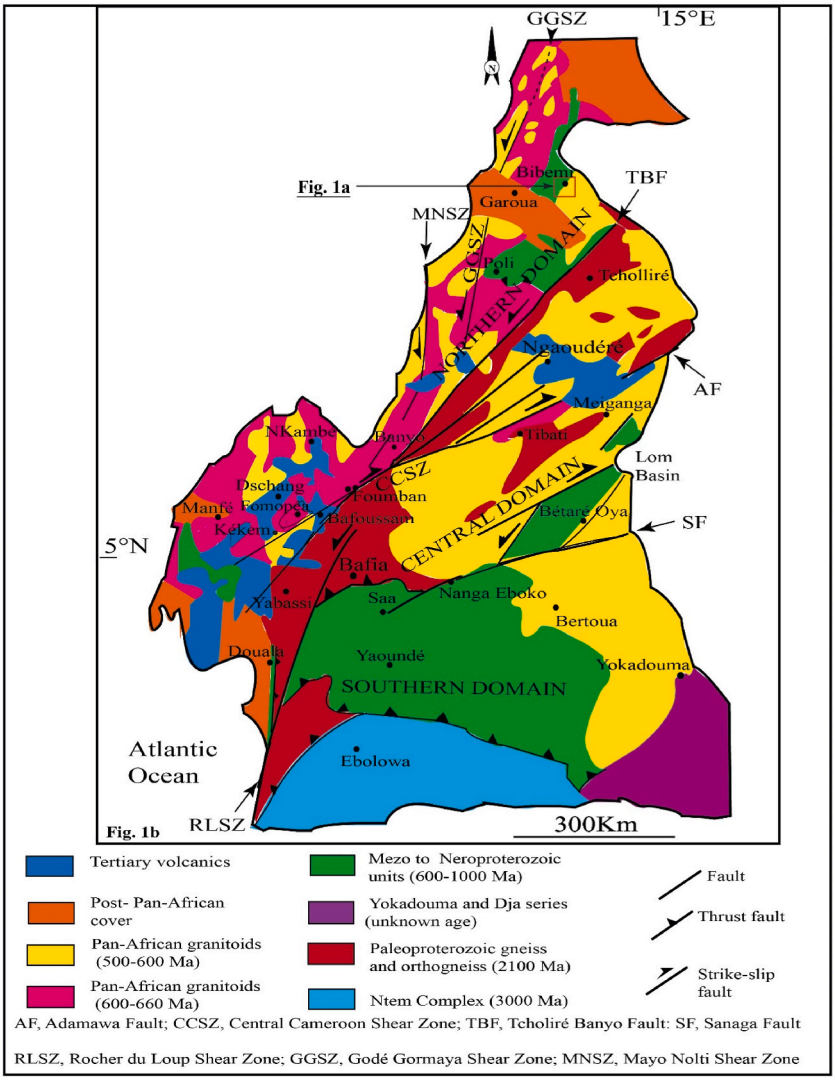

Fig. 1. (a) Location of the study area. (b) Geological map of north Cameroon (modified from Ref. [36]). The red rectangle represent study area. (For interpretation of the references to colour in this figure legend, the reader is referred to the Web version of this article.)

been extensively used for identifying and mapping subsurface minerals and structural features in regions of appropriate exposure like detection of hydrothermal alteration zones in tropical and subtropical regions using satellite remote sensing data including Landsat ETM+, Hyperion and PALSAR for gold mineralization [37,38,44–46,51,56].

Remote sensing methods have given useful instruments for characterising and identifying rock units, structures, and geological characteristics that have assisted in the determination of mineralization areas. Due to its high spatial, spectrum, and radiometric precision, remote sensing-based data is useful for mineral resource explorations. Delineating alteration regions and identifying mineral signatures are among the main goals of this research using satellite imagery [1,6,31,35,50,54]. To determine potential mineral reserves sites and alteration areas their quality must be defined [2,6,14,35,50,54,57]. This is because such a process is usually associated with the economic accumulation of metal ores such as copper (Cu), gold (Au), and silver (Ag). Numerous research articles such as remote sensing for mineral exploration [49], application of remote sensing techniques in lithological and mineral exploration [35], and mapping and discrimination the mineralization potential in the granitoids from Banyo area [50], used multi-spectral data (Landsat thematic mapper, Landsat 8 and 9 OLI) from satellites thus, defining the extent of altered regions, identifying altered and unaltered lithological units, and targeting ore forming regions.

Hydrothermal alteration minerals linked with orogenic gold and porphyry copper-gold formations have been extensively studied using improved multi-spectral as well as hyper-spectral imageries in the VNIR (visible-near-infrared), and SWIR (short-wave infrared) regions [3–5,7,9,16–18,23,27,30,37,38,47,53,56,62,65]. Particularly, hydrothermal alteration auras linked with ore formations exhibit absorption characteristics of Fe^{2+}, Fe^{3+}, Al–OH, Mg–OH, Si–OH, and CO_3^{2-} [37,44–46,56]. As a result, alteration mapping constitutes one of the most significant methods in the survey stage of natural resource discovery for such systems [3,9,30,35,40–43,53,56,65].

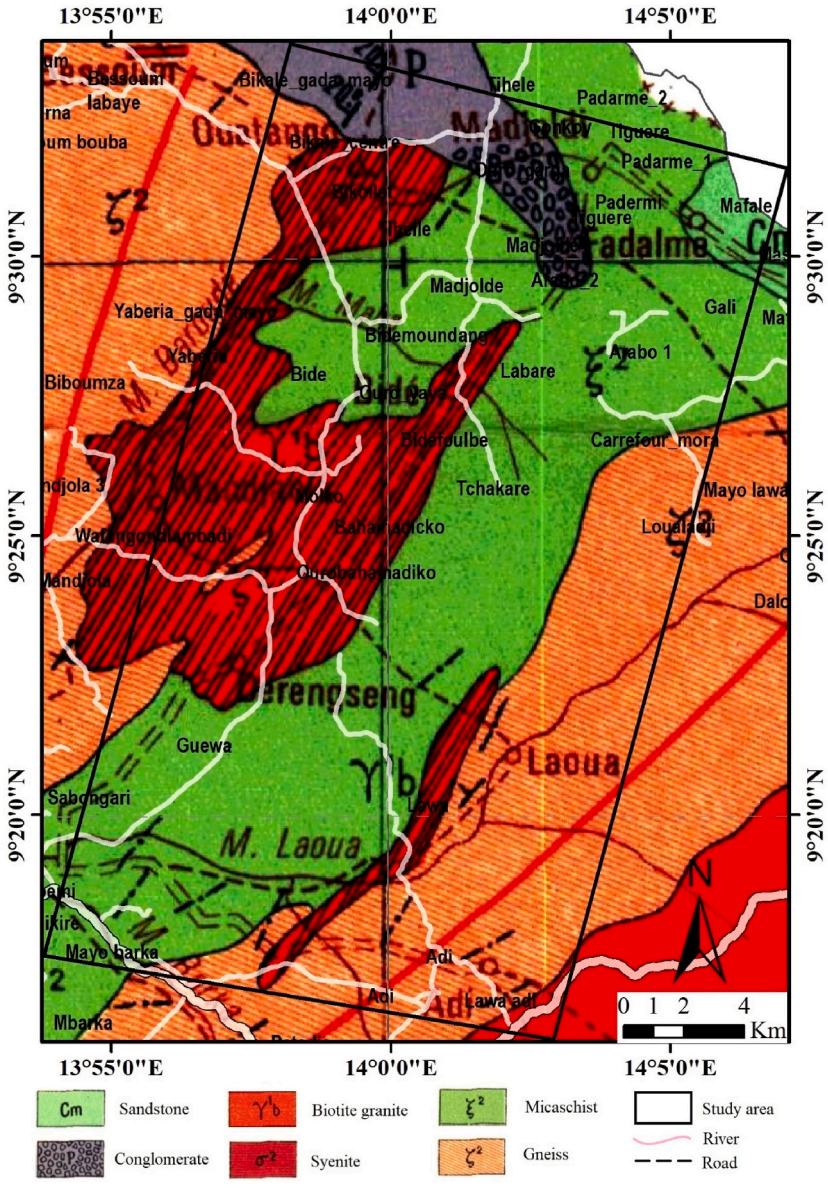

Fig. 2. Geological map of Bibemi area extracted from the geological map (1/200 000) of Garoua area from the Directory board of mines and geology of Cameroon [52].

Landsat 8 and 9 OLI (operational land imager) images have been used to process, assess and map lithological units, structures, and alteration minerals using digital image processing approaches [6,35,50]. Furthermore, these processing approaches include false colour composite (FCC), band ratios (BR), principal component analysis (PCA; standard and selective), and spectral angle mapper (SAM). Using a GIS-based method, such as fuzzy logic, to create mineral prospect maps based on satellite data has indeed become a quick and accurate instrument for finding target regions for mineral exploration [1,6,30,56], especially during the survey stage. This is due to the fact that using a GIS technique to merge geographically dispersed remote sensing data is an important strategy to mineral discovery because it enables the merging of various data using digital overlay techniques to maximise mineral targets [6,12,30,56].

Furthermore, the innovative aspect of this research is integrating fuzzy-logic technique, Landsat 9 OLI data and fieldwork investigations for enhancing prospective zones of gold mineralization by reducing the effective cost and time for field investigations. As a result, the primary objective of this study is highlighting prospective zones of gold mineralization in the Bibemi district and the secondary objectives are: (i) process and assess Landsat-9 data to maximise susceptibility of the maps to hydrothermal alteration minerals linked with gold mineralization in a vegetated tropical area (ii) conduct a thorough field investigation to confirm links between Landsat 9 fingerprints and hydrothermal alteration areas linked with gold mineralization; (iii) produce prospect maps and particularly locate high-probability areas in the Bibemi goldfield at local level for potential gold exploration.

Table 1
Landsat 9 OLI/TIRS data spectral characteristics (https://www.usgs.gov/landsat-mission).

Satellite	Sensor	Band (Wave length (μm))	Spectral region	Spectral resolution (m)	Covering size (km)
Landsat 9	OLI/TIRS	1 (0.43–0.45)	Coastal aerosol	30 m	185 km
		2 (0.45–0.51)	Blue		
		3 (0.53–0.59)	Green		
		4 (0.64–0.67)	Red		
		5 (0.85–0.88)	Near IR (NIR)		
		6 (1.57–1.65)	SWIR		
		7 (2.11–2.29)	SWIR		
		8 (0.50–0.68)	Panchromatic	15 m	
		9 (1.36–1.38)	Cirrus	30 m	
		10 (10.60–11.19)	Thermal Infrared (TIRS) 1	100 m	
		11 (11.50–12.51)	Thermal Infrared (TIRS) 2		

2. Location and regional geologic setting

The study area is situated in northern Cameroon between latitudes N9°15′0″ to N9°35′0″ and longitudes E13°53′0″ to E14°10′0” (Fig. 1a), specifically in the Benoue district, and has a total surface area of 2535 km^2. It is bounded in the north by the Figuil and Guider districts, in the south by the Lagdo and Rey-Bouba districts, and in the east and west by the Republic of Tchad, Pitoa, and Dembo regions, respectively.

The Bibemi area belongs to the north-western Cameroonian domain (Fig. 1b). The domain is composed of: (i) Medium to high grade Neo-Proterozoic (700 Ma) schists and gneisses of the Poli-Léré group that were developed during the setting of a magmatic arc [15,32,60]; (ii) pre-, syn-, and late-tectonic Pan-African calc-alkaline granitoids deposited between 660 and 580 Ma [15,32,36,58]; (iii) post-tectonic alkaline granitoids made up of mafic and felsic dykes intersected by intruding granites and syenites [15,32]; (iv) numerous basins composed of unmetamorphosed sediments and volcanic materials [15,59,61]. Isotope dating suggests that the majority of the gneissic and granitic formations in this domain are Neoproterozoic in age, with a small Paleo-proterozoic addition, in contrast to the Adamawa-Yade domain’s abundance of Paleo-proterozoic dates. This indicates that the Tcholliré-Banyo shear zone is a significant barrier dividing a young Neo-proterozoic upper crust on the west part from ancient formations on the eastern side [10,15,32,58].

Structurally, the Tcholliré-Banyo shear zone continues further east in the Mayo Kebbi area (southern Chad), is thought to highlight a crustal scale fissure [15,29,32]. This lineament has lately been regarded as a significant structural feature of the Sahara Metacraton [11,15,32], possibly corresponding to the eastern limit of the Saharan metacraton’s Chad cratonic core [15,26,32].

According to the earlier geological map (1/200 000) from the Directory board of mines and geology of Cameroon, the Bibemi area consist of a series of rocks such as sandstones, conglomerates, biotite granites, syenites, mica schist, and gneiss (Fig. 2, [52]). The NE-SW elongated biotite granites and syenites intrude mica schist and gneiss basement (Fig. 2, [52]).

3. Material & methods

3.1. Data and pre-processing

Cloud free L1T Landsat 9 OLI data (path/row: 184/054) obtained on January 3rd, 2023 covering Bibemi area, downloaded from USGS (United States Geological Survey) website (https://earthexplorer.usgs.gov) was used in this research for targeting rock units and detecting hydrothermal alterations linked to gold mineralization. The data is georeferenced to the Universal Transverse Mercator (UTM) 33 N using the WGS-84 datum. Table 1 lists the technical properties of the Landsat 9 data. The Landsat 9 OLI data consist of a collection of nine spectral bands (bands 1–9) and two TIR (thermal infrared) bands (bands 10–11). However, in this study the visible near-infrared (VNIR), shortwave infrared (SWIR), and panchromatic band (b8) of Landsat 9 were used. Moreover, the Landsat 9 cirrus (b 9) and TIR bands were not exploited in this research.

Radiometric calibrations and Quick atmospheric corrections (QUAC) algorithms using Envi 5.3 software were applied to the VNIR-SWIR Landsat 9 bands for good accuracy detection, because QUAC performs a more approximate atmospheric correction than other methods (e.g. FLAASH), typically yielding reflectance spectrum that are between 10 % and 15 % of the ground truth [8]. To enhance the quality of the initial data, the research area’s Landsat 9 data was processed using the Envi 5.3 software and hence, the obtained results were enhanced for visual assessment using layer staking and sub-setting.

In addition, a geological map of the Garoua area at a scale of 1/200 000 was utilised as a foundational source for comparison with the remote sensing data. Likewise, field data including field photographs of exposed rocks, gold samples, sampling points, and rock samples were respectively recorded and collected for eventual thin sections analysis at the Centre for Geological and Mining Research (CRGM) of Garoua, Cameroon.

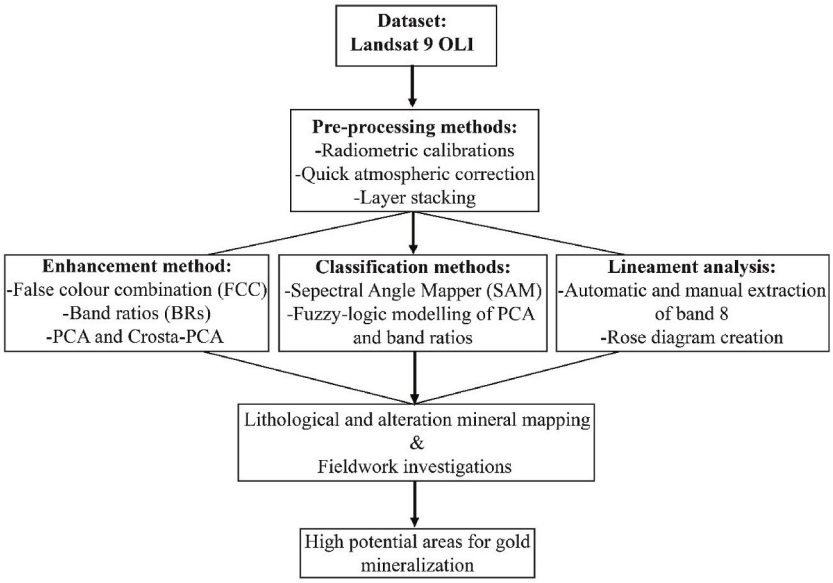

Fig. 3. Methodological flowchart.

3.2. Methods

The summary of consecutive methods for image processing are provided in Fig. 3. The diverse rock units, alteration minerals and structural features within the research area were distinguished using false colour composite (FCC), band ratios (BRs), standard and selective (Crosta) principal component analysis (PCA), spectral angle mapper (SAM) classification approach, lineament analysis, and fuzzy logic modelling. Accuracy assessment was performed for the SAM classification approach. The processing time was shortened due to image sub-setting.

3.2.1. False colour combination (FCC) and band rationing (BR)

FCC, frequently referred to as the Red-Green-Blue (RGB) composite technique, is a useful approach for enhancing objects beneath the surface and visually interpreting multi-spectral satellite images [34]. In this study, a combination of three bands (743, in RGB) was created to highlight and discriminate the main lithological units within the study area (Fig. 4).

BR is an essential image enhancement approach for improving surface details or features in multi-spectral images. To create a distinct spectral signature in the image, the process is utilised to eliminate the influence of light and topography [21]. Furthermore, it is a method that divides a single band by another in order to emphasise characteristics that are not visible in raw bands [39]. Two composite referenced BRs (4/2, 6/7, 6/5 and 7/5, 5/4, 6/7) have been generated or tested using the 'Band ratio algebra' tool in ENVI 5.3 software for discrimination and mapping of the extensively exposed lithological units within the study area using Landsat 9 OLI bands. On the other hand, for mapping alteration minerals, several referenced BRs such as 4/2 (for iron-oxide), 6/5 (for ferrous), 6/7 (for hydroxyl), 6/5*4/3 (iron rich mineral index) and a combination (4/2, 5/4, and 6/7) image of Landsat 9 OLI bands were generated. In addition, NDVI (Normalized Difference Vegetation Index) was calculated as NDVI = (5-4)/(5 + 4) and applied to identify vegetation within the study area.

3.2.2. Principal component analysis (standard and Crosta-PCA method)

According to Refs. [28,30,35], PCA seeks to generate uncorrelated bands, minimise the dimension of multi-spectral data, and separate noise parts. The PC analysis was performed using the PCA-rotation algorithm in ENVI 5.3 software. Standard PCA was applied on six bands of Landsat 9 OLI data including band 2, 3, 4, 5, 6, and 7 for lithological unit discrimination and mapping. The PC result file produced six sets of PC bands, including PC1, PC2, PC3, PC4, PC5, and PC6. Typically, the initial three bands involve the most information, whereas the last band contains noise data. A PCA combination (PC123) image was created for lithological interpretation. Likewise, Crosta-PCA method (selective PCA; [13]) was performed on two sets of Landsat 9 OLI data such as 2, 4, 5, 6 and 2, 5, 6, 7 for highlighting and targeting iron-oxide and hydroxyl minerals respectively. The Crosta PC analysis generated four sets of PC bands including PC1, PC2, PC3 and PC4. Thus, PC4 was used to target and enhance alteration minerals for each aforementioned Landsat 9 OLI Crosta-PCA sets.

3.2.3. Spectral angle mapper (SAM) and accuracy assessment

SAM algorithm is a supervised classification method in ENVI 5.3 software that works by matching the spectrum of pixels to the selected reference spectra. SAM examines the angle of reference spectra vector and every single pixel vector in n-D area, with lower angles representing closer matches to the reference spectra [25]. In this study, the SAM approach was computed on band 743 of

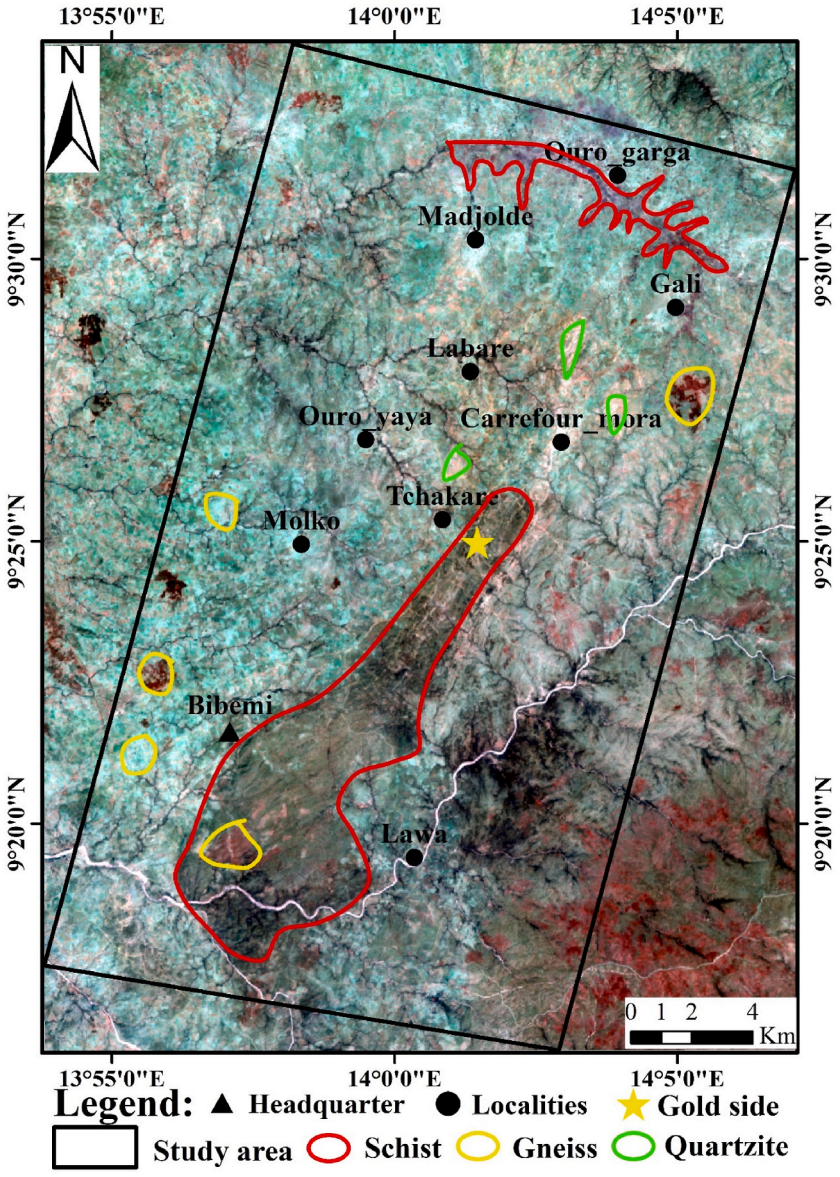

Fig. 4. False colour combination image of Landsat 9 OLI (743) discriminating several rock units in Bibemi area. (For interpretation of the references to colour in this figure legend, the reader is referred to the Web version of this article.)

Landsat 9 OLI data and was based on the selected reference spectra from the United States Geological Survey (USGS) laboratory spectra library. The n-D analysis was used to extract spectra from the image. Accordingly, ENVI 5.3 confusion matrix algorithm was used to assess the accuracy of SAM classification approach. As a result, the overall accuracy (OA) and kappa coefficient were determined and represent the whole accuracy result.

3.2.4. Lineament mapping

GIS and remote sensing methods were used to analyse and interpret lineaments. In this study, lineaments were elicited both automatically using the PCI Geomatica line extraction tool algorithm and manually through visual interpretation of pan-chromatic band (band 8) of Landsat 9 OLI data. However, the resultant lineaments were exported as GIS shapefiles and imported into ArcGIS 10.3 programme for analysis and processing using GIS line density and statistical approaches. Thus, the lengths of each lineaments were calculated as well as the determination of their directions/trends, which are therefore plotted on a rose diagram using Rockworks line tool algorithm for kinematic interpretations.

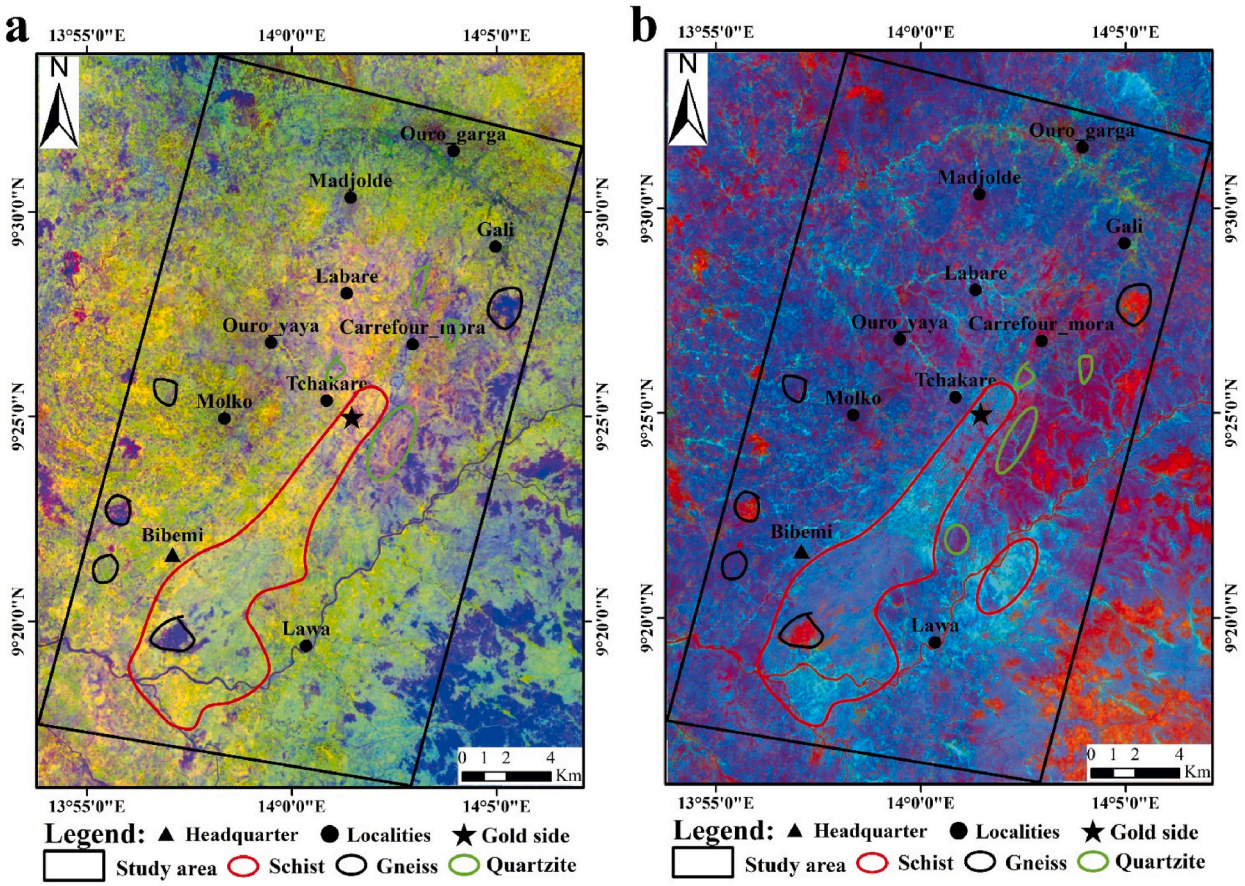

Fig. 5. Band ratios images of Landsat 9 OLI data illustrating rock units and alteration zones in Bibemi area: (a) Sabin ratio (4/2, 6/7, 6/5 in RGB) and (b) Kaufman ratio (7/5, 5/4, 6/7 in RGB).

3.2.5. Fuzzy-logic modelling technique

Fuzzy-logic modelling technique is a type of several-valued logic in which the actual values of the variables might be any real number ranging from 0 to 1 [33]. In this study, using the fuzzy linear membership function from ArcGIS 10.3.1 software, fuzzy maps were classified into 10 suitable class sets and thus, fuzzified. Furthermore, the fuzzy AND function was performed for thematic input layers obtained from BR and PCA analyses of Landsat 9 OLI data.

3.2.6. Fieldwork survey

Fieldwork investigations was conducted on under good climate conditions mainly during the dry season in February 2023. This survey within the study area was carried out using GPS (Global Positioning System) to validate remote sensing results including rock units bearing alteration minerals related to gold mineralization. Furthermore, mining gold sites were observed on the field, their positions were recorded and samples collected for petrographic observations at the Geological and Mining Research Centre Laboratory (GMRC) of Garoua, Cameroon.

4. Results

4.1. Lithological mapping

As a lithological discrimination approach, mapping frequently uses remote sensing coupled with geographic information system (GIS).

4.1.1. False colour combination (FCC)

In this study, VNIR-SWIR bands of Landsat 9 OLI data were used to generate a unique FCC image. Bands 7(2.11–2.29 μm), 4 (0.64–0.67 μm), and 3(0.53–0.59 μm) of Landsat 9 data were allocated to the RGB composite image to discriminate geological features. The resulting FCC (7, 4, and 3) image of the research area is shown in Fig. 4. Thus, rock units contacts were differentiated (Fig. 4). Spectrum properties of various metamorphic rocks such as schists, gneisses and quartzite can be identified. The FCC (7, 4, and 3) image

Table 2
Landsat 9 OLI data PCs eigenvectors and eigenvalues loading results.

Eigenvectors	Band 2	Band 3	Band 4	Band 5	Band 6	Band 7	Eigenvalues	Variance (%)
PC1	0.13	0.14	0.23	0.37	0.70	0.53	3190930.89	86.54
PC2	0.01	0.08	0.17	0.74	0.02	−0.65	412165.69	11.18
PC3	0.32	0.31	0.42	0.22	−0.66	0.38	60690.73	1.65
PC4	0.35	0.27	0.56	**−0.51**	**0.27**	−0.39	18822.39	0.51
PC5	−0.86	0.08	0.50	−0.06	−0.04	0.06	3033.4	0.08
PC6	0.16	−0.89	0.41	0.04	−0.04	0.04	1644.64	0.04

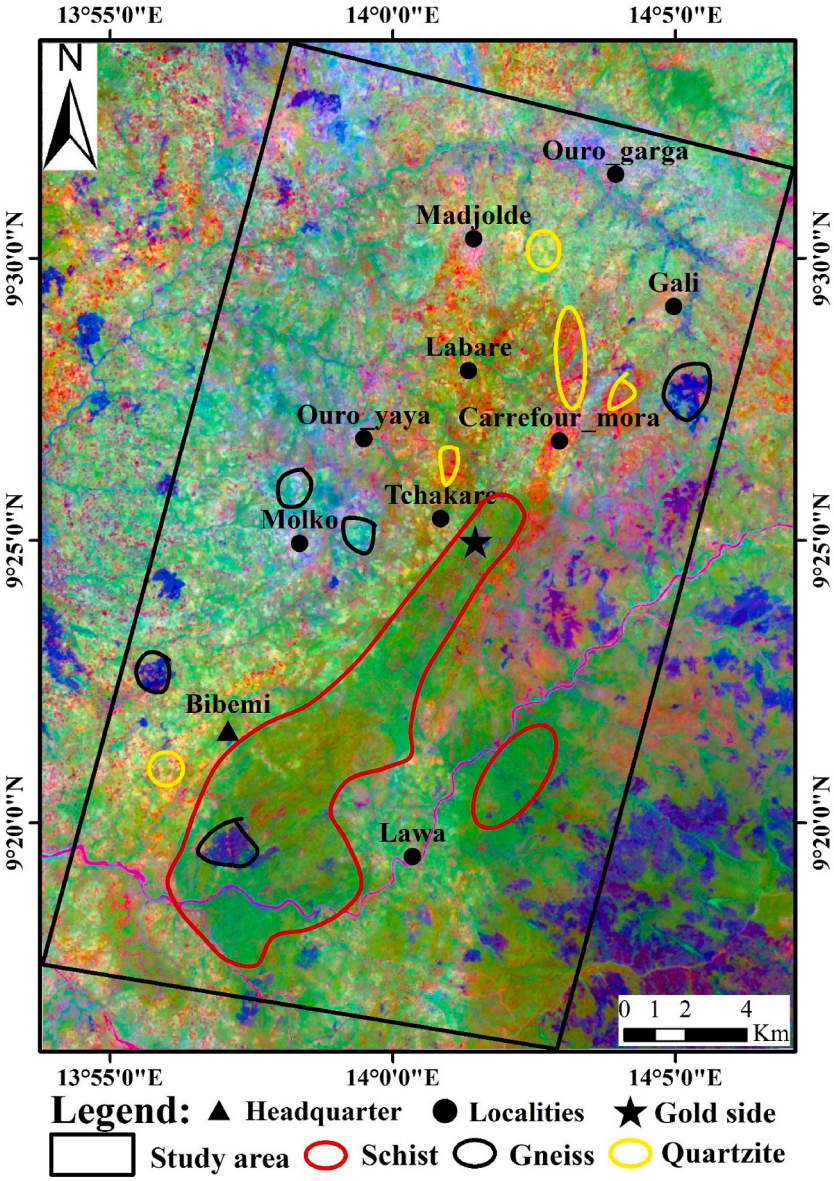

Fig. 6. PCA (PC1, 2, 3) combination images of Landsat 9 OLI data targeting rock formations in Bibemi area.

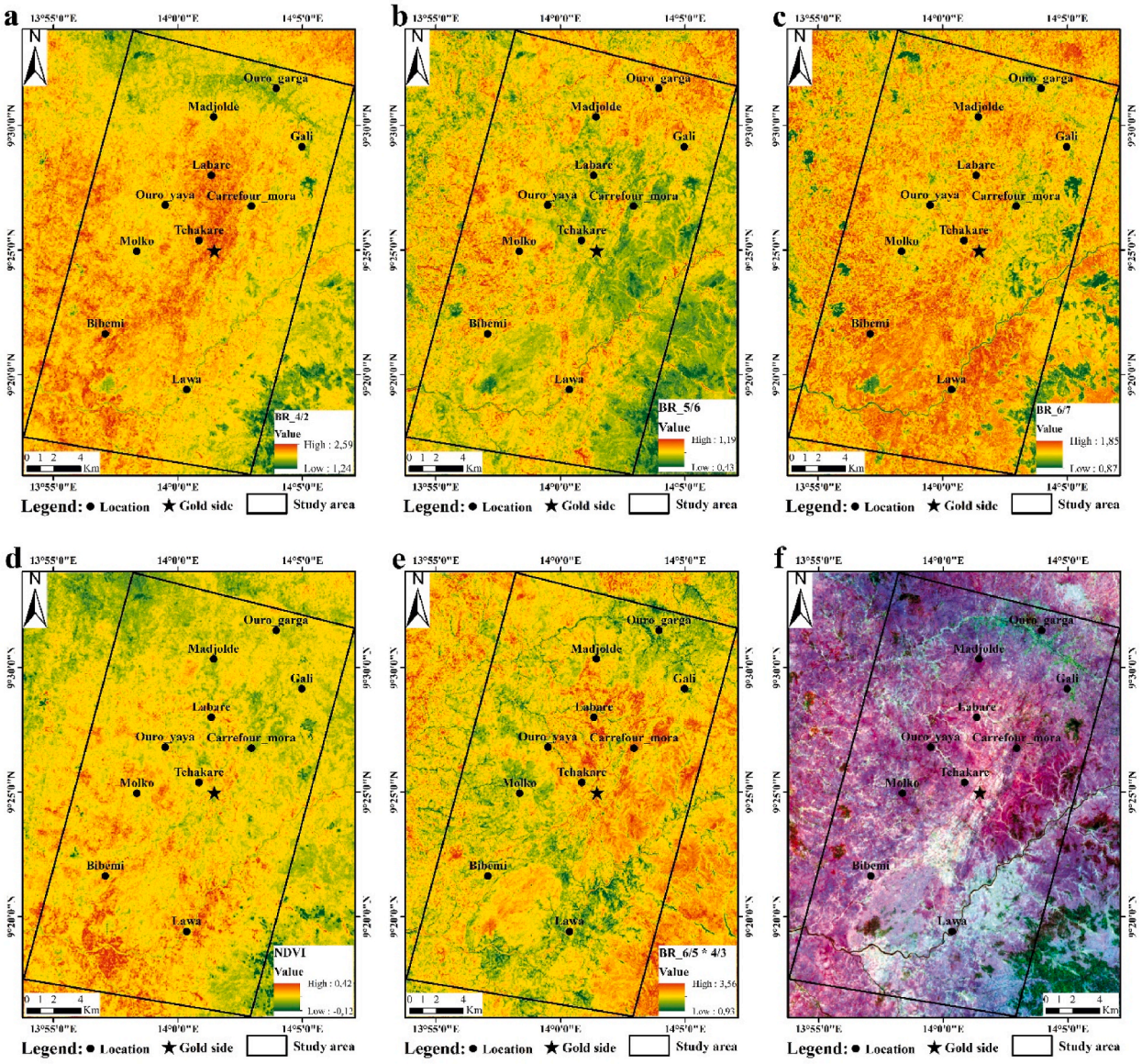

Fig. 7. Band ratios images of Landsat 9 OLI data targeting alterations minerals related to gold mineralization and vegetated zones in Bibemi area: (a) BR 4/2 mapping iron-oxide; (b) BR 5/6 targeting unaltered rocks and silicate or ferrous minerals; (c) BR 6/7 illustrating OH-bearing and carbonate minerals; (d) NDVI; (e) iron rich mineral index; and (f) RGB combination of BRs (4/2, 5/4, and 6/7) for hydrothermal alteration mineral mapping. (For interpretation of the references to colour in this figure legend, the reader is referred to the Web version of this article.)

depicts the schist units as dark brown to brown and purple colours, the variety of gneisses display cyan, green, and red tones, quartzite show bright colour pixel and water as black pixels (Fig. 4).

4.1.2. Band ratios (BR)

Two distinct BRs composites (4/2, 6/7, 6/5 and 7/5, 5/4, 6/7) were produced to discriminate rock units and potentially alteration zones in the study area. Depending on spectral properties of alteration minerals, these BRs were assigned to the RGB combination for rock unit discrimination and mapping. Fig. 5a illustrate three main rock units and altered areas in the study area resulting from the Sabin BRs combination (4/2, 6/7, and 6/5 in RGB). Hence, schist units were represented as yellow pixels, the gneiss units display blue and green tones, and quartzite depicts purple pixels, altered areas show bright pixels (Fig. 5a). Fig. 5b is the resultant image from Kaufman BRs combination (7/5, 5/4, and 6/7 in RGB). It depicts altered schist rocks as cyan tones, altered gneisses display blue and red tones, and quartzite units show purple pixels (Fig. 5b). Some alteration areas depicts green pixels (Fig. 5b).

Table 3
Landsat 9 OLI PCs data loadings of band 2, 4, 5 and 6 for Iron-oxide minerals.

Eigenvector	Band2	Band4	Band5	Band6	Eigenvalues	Variance %	Surface
PC1	0.114739	0.192155	0.486706	0.844410	22774606.06	98.92	albedo
PC2	0.182892	0.251040	−0.856703	0.411812	169164.94	0.73	vegetation
PC3	0.502706	0.775286	0.169811	−0.342610	71692.49	0.31	vegetation
PC4	**−0.837061**	**0.546797**	−0.018487	−0.000034	7062.37	0.03	Iron-oxide

Table 4
Landsat 9 OLI PCs data loadings of band 2, 5, 6 and 7 for Hydroxyl minerals.

Eigenvector	Band2	Band5	Band6	Band7	Eigenvalues	Variance %	Surface
PC1	0.099453	0.417205	0.729584	0.532688	30539027.03	98.68	albedo
PC2	0.078452	−0.752296	−0.056330	0.651708	344522.41	1.11	vegetation
PC3	0.406860	0.471997	−0.646608	0.439980	43734.76	0.14	vegetation
PC4	−0.904665	0.192900	**−0.215482**	**0.312950**	20933.37	0.07	Hydroxyl/Carbonate

4.1.3. Principal component analysis (PCA)

PCA analysis was performed on bands 2, 3, 4, 5, 6 and 7 of Landsat 9 OLI data. The PCA results (Table 2) demonstrated that PC1 exhibits the greatest percentage of the variance (86.54 %), while PC6 displays relatively minimal variance (0.04 %) due to noise in the initial spectral bands of Landsat 9 data. Landsat 9 PCA image (PC1, 2, and 3) was effective in discriminating the various rock units of the study area (Fig. 6), where schist units were represented by green pixels, gneisses appear with cyan and blue colours, and quartzite units exhibit red and yellow to bright tones (Fig. 6).

4.2. Mineral mapping

4.2.1. Band ratio (BR) and false colour composite (FCC)

Mapping of alterations minerals related to gold mineralization was achieved using some BRs (4/2, 6/7, and 5/6) of Landsat 9 OLI data depending on their laboratory spectral features. Fig. 7a illustrates Landsat 9 BR (4/2) image as red pixels, used to map iron-oxide or hydroxide minerals. The BR 5/6 of Landsat 9 was applied to depict unaltered rocks and silicate or ferrous minerals like pyroxenes and olivine due to their spectral signatures. Thus, this BR (5/6) image indicates the concentration of ferrous/silicate minerals as red pixels (Fig. 7b). The Landsat 9 BR (6/7) image, used to map OH-bearing and carbonate minerals, yields results that seems to reveal clay and carbonate minerals as red tones that are notably localized in and around the gold mineralized site, including vegetation cover (Fig. 7c). To distinguish between alteration minerals and vegetative cover, the NDVI (Normalized Difference Vegetation Index) was determined using the BRs (5-4)/(5 + 4) of Landsat 9 data (Fig. 7d).

Additionally, for comparison purposes iron rich mineral index [Fe-MI: (6/5) × (4/3)] and BR combinations (4/2, 5/4, and 6/7) were used. The Fe-MI [(6/5) × (4/3)] of [42], depicts red tones (Fig. 7e). Moreover, BRs combination (4/2, 5/4, and 6/7) of Landsat 9 displays iron oxide minerals as purple to red colours, ferrous minerals as white tones, and OH-bearing minerals appear with cyan colours (Fig. 7f).

4.2.2. Crosta-PCA (principal component analysis)

In this study, Crosta-PCA known as the selective PCA technique was performed on bands 2, 4, 5, 6 and bands 2, 5, 6, 7 respectively to detect iron-oxide, and hydroxyl bearing/carbonate minerals due to their higher band loadings which can be utilised as an indicator for alteration mineral deposits thus, most effective in enhancing hydrothermal alteration minerals. The PCA results (Tables 2–4) obtained from standard and Crosta-PCA analysis of Landsat 9 data demonstrates that some PC images include key details that may be regarded as representations of ferrous/silicate minerals, iron-oxides, hydroxyl/carbonate minerals, and vegetation.

To target ferrous/silicate minerals achieved from standard PCA analysis, Table 2 indicates that PC4 contain significant data. The eigenvector loadings of PC4 illustrate the moderate negative contributions of b5 (−0.512294) and positive contributions of b6 (0.267166). Hence, ferrous/silicate minerals exhibit red pixels (Fig. 8a). Ferrous/silicate minerals were seen in gneiss and quartzite units.

Table 3 displays eigenvector loadings of PC bands 2, 4, 5, and 6 for iron-oxide mineralization. PC4 illustrates positive contributions in b4 (0.546797) and high negative contributions in b2 (−0.837061). Thus, iron-oxide mineralization were targeted in gneisses, quartzite and some schist units as red tones (Fig. 8b).

Moreover, hydroxyl bearing and carbonate (H/C) minerals were obtained from selective or Crosta PCA analysis of Landsat 9 OLI data (2, 5, 6, and 7) as illustrated in Table 4. Accordingly, these minerals were targeted in PC4 which demonstrates a great negative eigenvector loading in b6 (−0.215482) and a high positive loading of b7 (0.312950). As a result, H/C mineral groups displayed green pixels on PC4 image due to the negative loading contribution of b6. Thus, the resulted PC4 image was negated or inverted (multiplied by −1; [13]) to obtain red pixels (Fig. 8c). H/C mineralization were spatially distributed and mapped in gneiss and quartzite rocks (Fig. 8c). In addition, Fig. 8d illustrates an RGB combination of iron-oxides (R), hydroxyl/carbonate (G), and ferrous (B) minerals for the study area as red, green, and blue to cyan respectively.

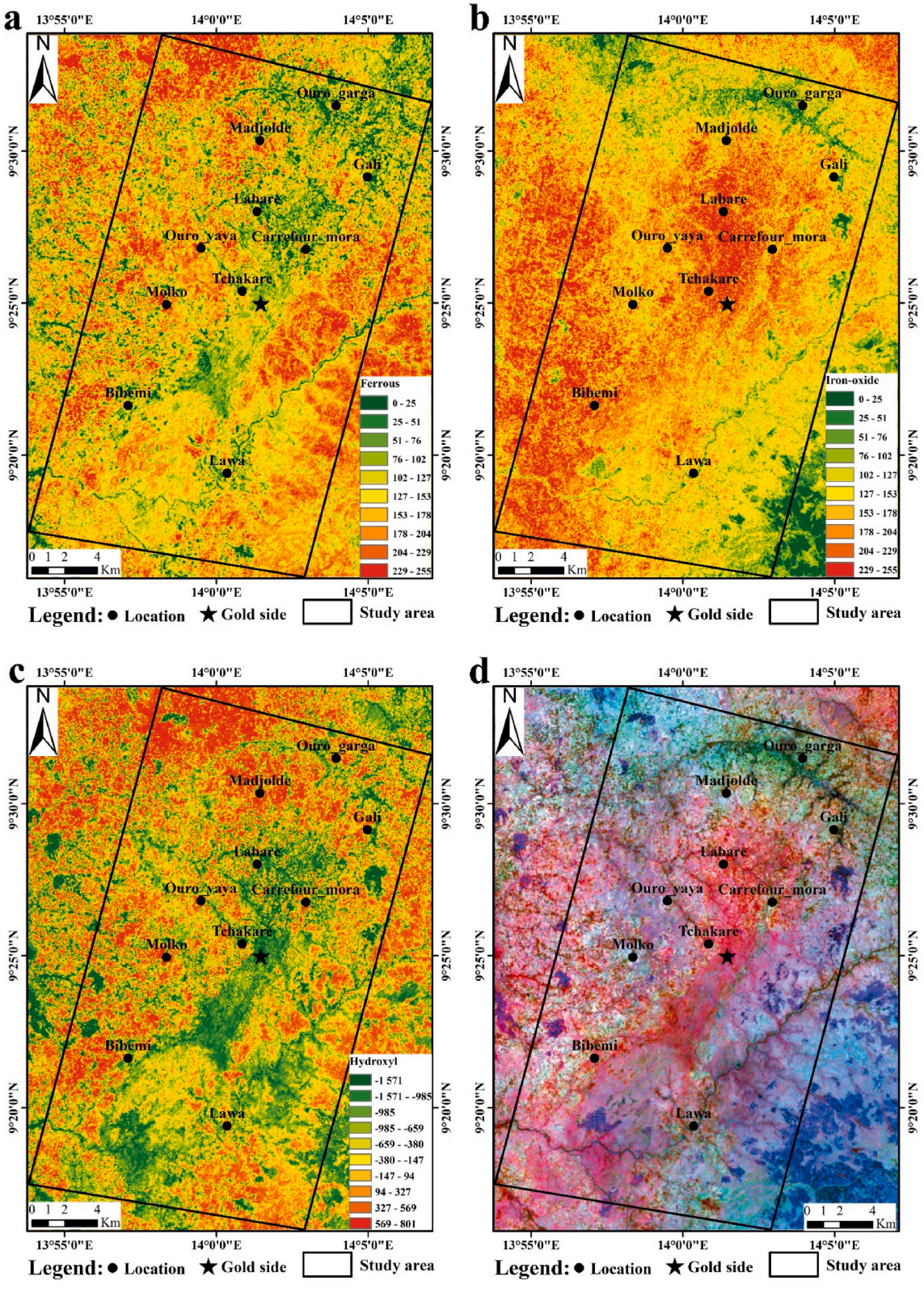

(caption on next page)

Fig. 8. Crosta-PCA combination images mapping of alterations minerals related to gold mineralization in Bibemi area: (a) PC4 illustrating ferrous/silicate minerals; (b) PC4 showing iron-oxide mineralization; (c) PC4 illustrating hydroxyl bearing and carbonate (H/C) minerals; and (d) RGB combinations of iron-oxides, hydroxyl/carbonate, and ferrous minerals respectively. (For interpretation of the references to colour in this figure legend, the reader is referred to the Web version of this article.)

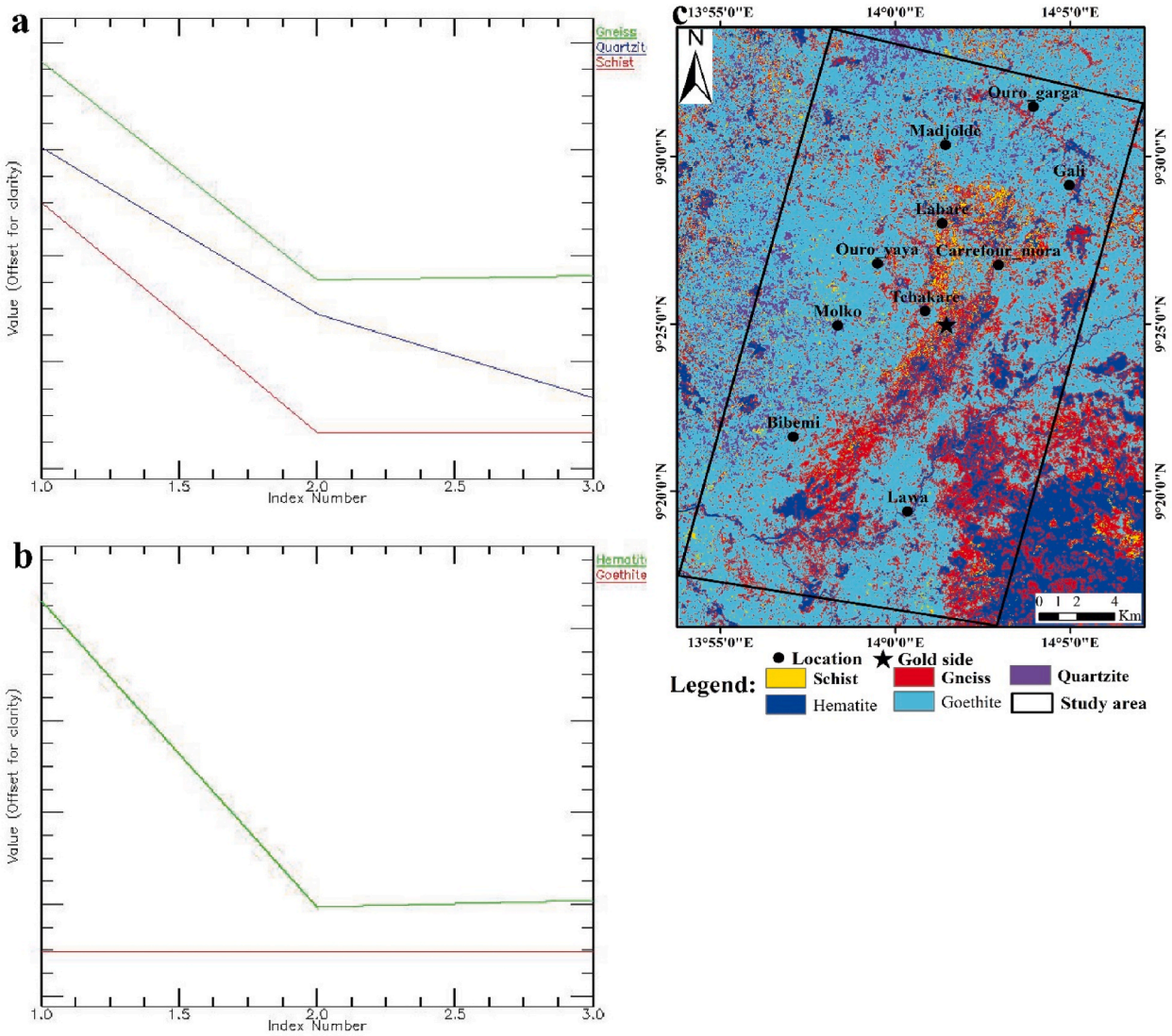

Fig. 9. (a–b) Spectral signatures of selected n-D classes (end-member spectra) and (c) SAM classification illustrating targeted alteration minerals related to gold mineralization in Bibemi area. (For interpretation of the references to colour in this figure legend, the reader is referred to the Web version of this article.)

4.3. Spectral angle mapper (SAM) method and accuracy assessment

To reduce the amount of unidentified pixels and avoid spectra interference with other minerals, the SAM approach was applied in accordance with the ideal threshold angle radians (0.2). The n-Dimensional analysis approach yielded three and two end member spectra for rock units and alteration minerals, respectively. For recognizing rock units bearing iron-oxides, hydroxyl/carbonates, and ferrous mineral groups, some notable similarities among spectral characteristics of the n-D classes and the targeted minerals are defined (Fig. 9a and b). Fig. 9c displays a map showing the research area's SAM classification detailing the regional dispersion of iron oxides, hydroxyl/carbonate, and ferrous minerals in rock units.

The confusion matrix of the output generated using the SAM classification approach is displayed in Table 5. According to several trial experiment, the overall accuracy of the SAM approach often approached 81.88 % with Kappa coefficient of 0.67. Hence, the SAM

Table 5
Confusion matrix of SAM classification.

Class	Schist	Quartzite	Gneiss	Goethite	Hematite	Total (%)	
Schist		10.57	0.09	0.30	0	0.42	0.33
Quartzite		3.57	36.18	0	0.09	0	1.67
Gneiss		20.89	0	49.40	0.80	21.81	10.13
Goethite		53.24	63.73	21.93	98.42	10.89	69.91
Hematite		11.72	0	28.38	0.69	66.88	17.95
Total		100	100	100	100	100	100
Overall Accuracy (%)		81.88					
Kappa Coefficient		0.67					

method demonstrated to be suitable for high spatial resolution image classification in the study area.

4.4. Lineaments analysis

In this study, Landsat 9 OLI panchromatic band (band 8) was used for lineament extraction that includes both manual and automatic extraction processed using PCI Geomatica 2015 and ArcGis software. Each lithological unit bears its lineament pattern, according to the lineament map and density map (Fig. 10a and b). The constructed rose diagram displays three structural directions (Fig. 10c): 1) the principal N–S direction, 2) a secondary NNE-SSW direction, and 3) an accessory ESE-WNW to SSE-NNW direction. The density map analysis of lineaments revealed that the important lineaments are dominant as red tones in the south-western, northern and south-eastern parts of the research area (Fig. 10b).

4.5. Fuzzy modelling

Using the most relevant alteration data maps obtained from PCA and BRs approaches, the fuzzy model was applied to generate mineral potential maps of the study area's attractive locations for gold mineralization (Table 6). The Landsat 9 PC4 bands (for iron-oxides, hydroxyl/carbonate and ferrous minerals), and BR of 4/2, 6/7, and 6/5 thematic maps were chosen and merged using the fuzzy AND operator to generate a local mineral potential map (Fig. 11d).

Fig. 11 shows the local mineral potential map of the study area. Evaluating the fuzzy membership of each alteration mineral indicates that the highest favourability index (0.8–1) is found in the west-centre (iron-oxides), south-eastern (ferrous minerals) and all (hydroxyl/carbonates) parts of the study area (Fig. 11a, b and c). The greatest value (0.9–1.0) of the favourable rating index was related with artisanal gold mining locations, according to the results of all fuzzy maps (Fig. 11d). At the local level, the alteration areas linked with structural contacts or quartz veins were the most promising potential locations for gold mineralization.

4.6. Outcomes of field investigation

A number of field photographs were obtained to demonstrate the position and features of the alteration areas and rock units (Fig. 12 a-d). Within a few meters of the surface, gold mineralization was found both in intrusion related mineralization areas (Fig. 12a), gravels (Fig. 12b), altered rocks, and quartz dominant vein systems linked with iron-oxide, hydroxyl, and carbonate minerals. Quartz, K-feldspath, tourmaline, albite, mica, and chlorite were also found in vein networks. The gold (Fig. 12c and d) is sourced from granitic rocks (Fig. 12b). In the Bibemi region (Fig. 12a), the quartz vein was abundantly exposed. Biotite was always widespread, whereas amphibole was usually little.

FCC, PCA and SAM were merged using GIS tools to create an updated geological map for the Bibemi area. The resulting geological map is depicted in Fig. 13 demonstrating that the study area was primarily composed of gneiss units comprising dominant hydroxyl/carbonate minerals, schist units containing major iron-oxide and ferrous minerals, and quartzite formations including both iron-oxides and hydroxyl/carbonate minerals.

5. Discussion

Investigation of gold deposits is expensive using field surveys and traditional techniques, but using satellite images is easier due to the sedimentary backdrop and host rocks of this form of gold deposit [30,37–39,55,56,64–66].

In this research, Landsat 9 OLI data from the Bibemi region were analysed and evaluated to identify high-probability areas for gold mineralization and to update the geological map of the study area. Using BRs, PCA (standard and selective), and SAM methods [19–23, 30,35,48–50,56]], the spatial distribution of iron-oxides, hydroxyl (clay and carbonate), and ferrous minerals linked with gold

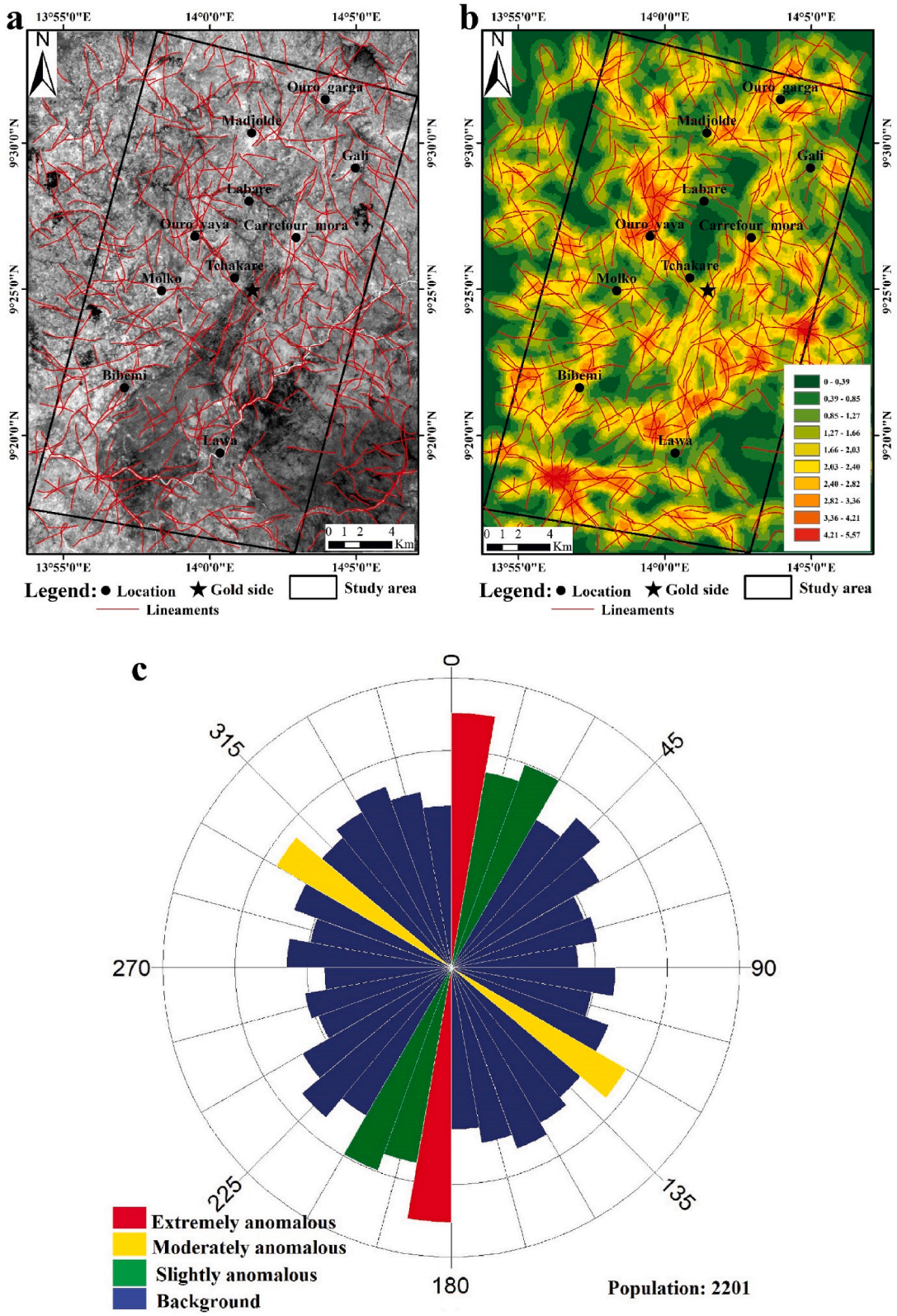

Fig. 10. Lineament mapping of Bibemi area: (a) lineament map; (b) lineament density map; and (c) rose diagram of lineaments.

Table 6
Fuzzy modelling parameters used for analysis.

Data	Input layers	Fuzzy membership type	Fuzzy operator	Target minerals
Landsat 9 OLI	PC4	Linear	AND	Iron-oxide
	PC4			Hydroxyl and carbonates
	PC4			Ferrous
	BR 4/2			Iron-oxide
	BR 6/7			Hydroxyl and carbonates
	BR 6/5			Ferrous

formations was mapped [30,56]. The results revealed that iron oxides are widely distributed in schist and quartzite formations. The hydroxyl/carbonate minerals are typically found in gneissic and quartzite formations. Ferrous minerals, on the other hand, are found in schists units. The fuzzy logic model [24,30,56,63] was used to generate potential maps of alteration minerals by integrating BRs and PCs alteration themed layers [30]. According to the observations, the regions with the greatest value of the favourable rating index are mostly found in the central and southern sections, as well as the north-eastern part of the research region (Fig. 11). Integrating FCC, PCA, and SAM data using GIS-based methods yielded a revised geological/mineralization map of the research area hence, a lithological-mineral map of the Bibemi area was created (Fig. 13). Moreover, the schist and gneiss formations at the central and southern parts were proposed as a high-potential formation in the research region, containing iron oxides coupled with hydroxyl/carbonates, and ferrous mineral units that can be deemed high-potential areas for future gold research in the study region. In addition, the relationship between lineaments, lithological units, and associated mineral deposits has been investigated in Bibemi area, through Landsat 9 OLI data (pan-chromatic band) analysis and geological fieldwork. The processing of the pan-chromatic band (band 8) of Landsat 9 OLI using GIS and remote sensing techniques revealed lineaments that are significant for interpreting mineralization channels within the study area. Hence, the major trends of lineaments (NNE-SSW and ESE-WNW) obtained from rose diagram assessment (Fig. 10c) correlates with litho-structural trends identified in the field and as seen in Fig. 13 thus, serving as pathways for mineralizing hydrothermal fluids related to gold mineralization. The identified corridors observed in Fig. 13 are potential gold-rich zones. The second corridor (ESE-WNW) that is mineralized but not yet identified in the field could be a new target area for gold prospecting (Fig. 13).

According to the digital image verification (SAM analysis) and fieldwork investigations, the alteration areas mapped by the Landsat 9 OLI bands have a better rate of understanding (Kappa coefficient of 0.67) and high precision (overall accuracy of 81.88 %) and contain alteration minerals such as hematite and goethite. As a result, the mineral locations of alterations outlined in this research were verified and dependable.

6. Conclusion

In the Bibemi region, Landsat 9 OLI data was analysed and examined for rock units and alteration minerals linked with gold mineralization.

By using the FCC, BRs, PCA, and SAM processing methods on the Landsat 9 data, the rock units were mapped. The results of analysing Landsat 9 data reveal important details about rock units when contrasted to the geological map of the area that can be used to update the previous geological map for the study region.

A comprehensive global distribution of alteration mineral groups (iron oxide, hydroxyl/carbonate, and ferrous minerals) was identified in the research region using BRs and selective PCA technique on the Landsat 9 dataset. The analyses showed that the major rock formations have varying abundance and distribution of alteration minerals, including signs of high prospective gold exploration areas. The high prospect areas are geographically found in the centre, southern portion and the research area's north-eastern portion. These high prospect areas should be considered for future thorough research and precise geological studies.

7. Consent for publication

We, the authors, give our consent for the publication of identifiable details, which can include figures/photographs and/or details within the text to be published in the above journal and article. We the authors confirm that we have seen and been given the opportunity to read the article to be published by Heliyon.

Availability of data and materials

The datasets generated during and/or analysed during the current study are not publicly available in a repository because it is part

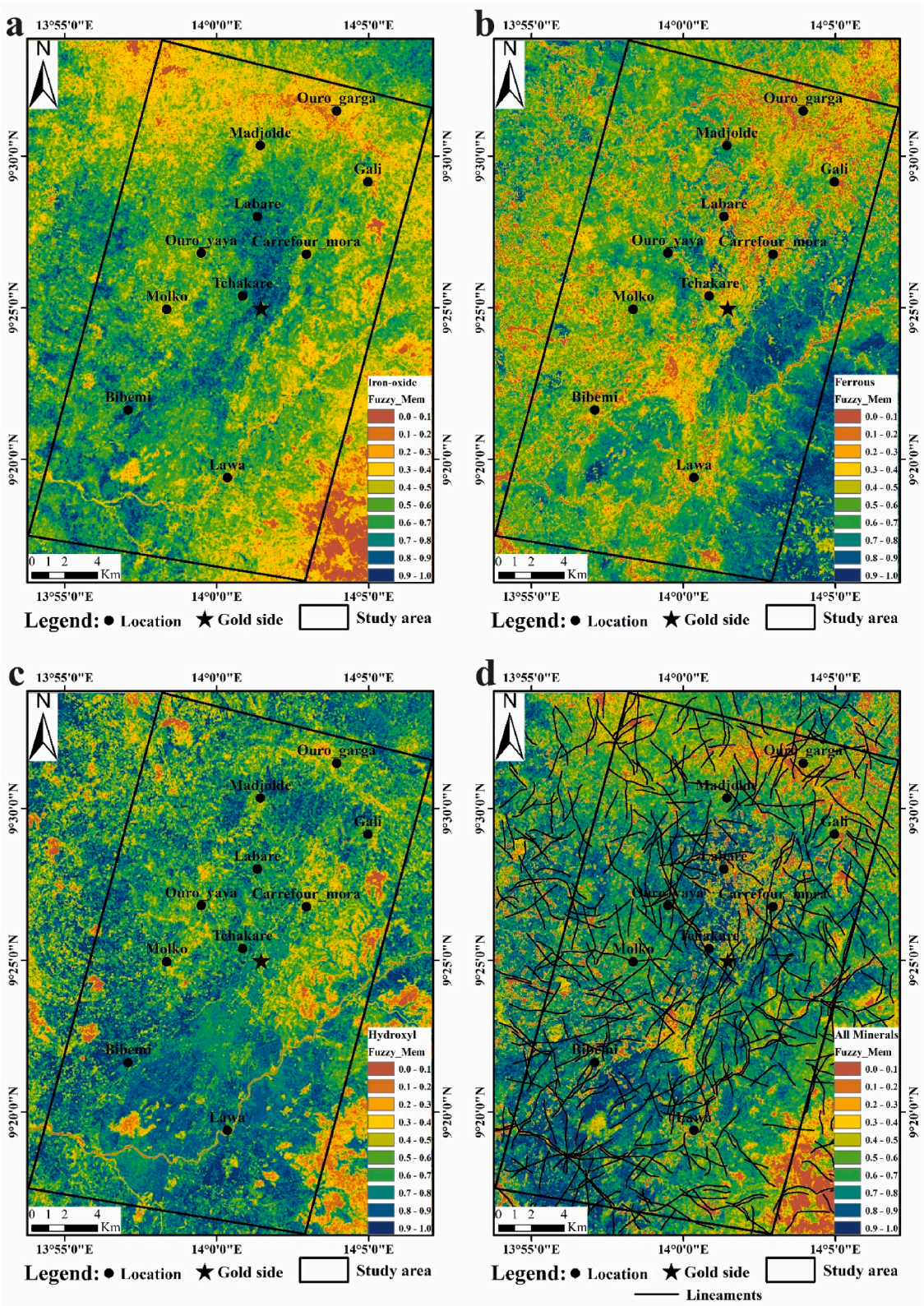

Fig. 11. Fuzzy maps illustrating potentially mineralized zones in the study area: (a) fuzzy map of iron-oxide minerals; (b) fuzzy map of ferrous minerals; (c) fuzzy map of hydroxyl minerals; and (d) fuzzy map of all hydrothermal alteration minerals related to gold mineralization. (For interpretation of the references to colour in this figure legend, the reader is referred to the Web version of this article.)

Fig. 12. Field pictures of gold prospective areas: (a–b) Bibemi artisanal gold mining site; (c) extracted gold using chemicals; and (d) transformed gold into ingot. (For interpretation of the references to colour in this figure legend, the reader is referred to the Web version of this article.)

of a PhD research work but would be available from the corresponding author on reasonable request.

Funding

No funding and grants was received for conducting this study or assist with the preparation of this manuscript.

Competing interest

The authors declare no conflict of interest for this work.

CRediT authorship contribution statement

Safianou Ousmanou: Writing - review & editing, Writing - original draft, Visualization, Validation, Supervision, Software, Methodology, Investigation, Formal analysis, Data curation, Conceptualization. **Yaya Fodoue:** Writing - review & editing, Writing - original draft, Visualization, Validation, Supervision, Software, Methodology, Investigation, Formal analysis, Conceptualization. **Jacques Wassouo Wadjou:** Validation, Supervision. **Amadou Diguim Kepnamou:** Validation, Supervision. **Eric Martial Fozing:** Visualization, Validation. **Maurice Kwékam:** Validation, Supervision. **Miranda Ikfi:** Writing - review & editing, Validation, Supervision.

Declaration of competing interest

The authors declare that they have no known competing financial interests or personal relationships that could have appeared to influence the work reported in this paper.

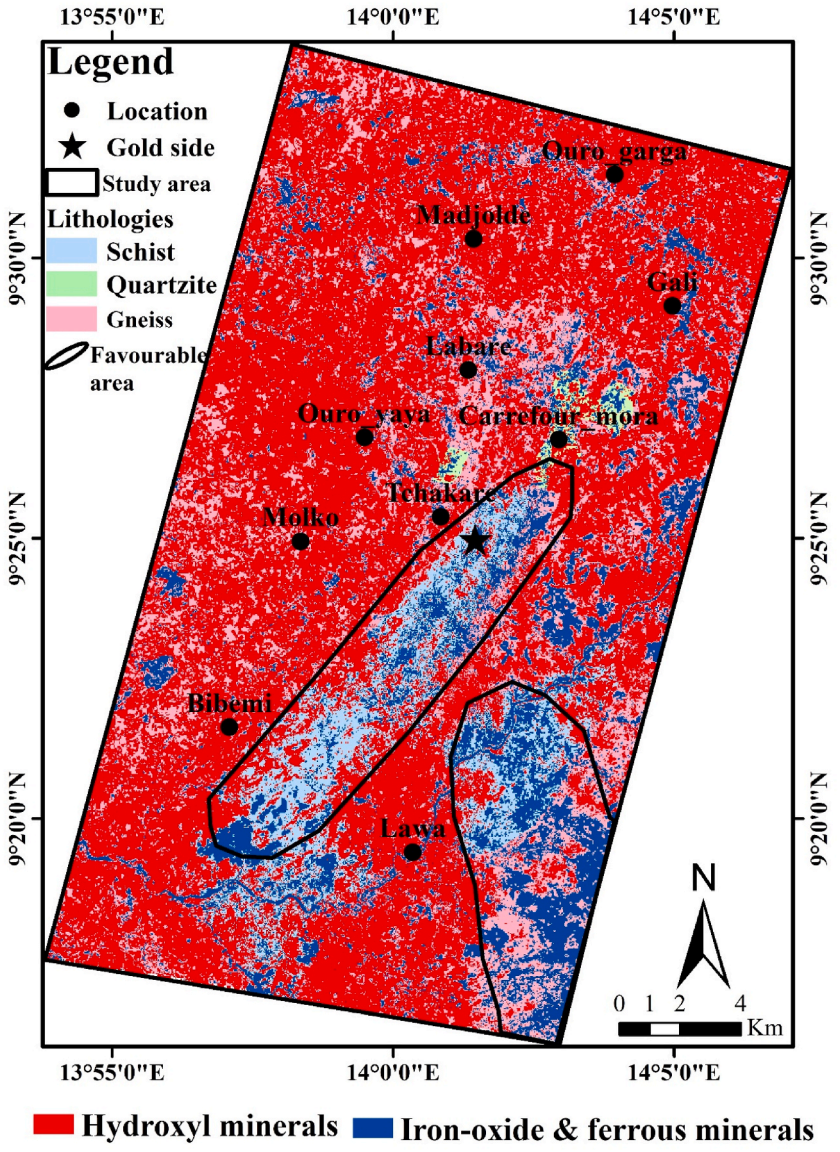

Fig. 13. An overview of the zones favourable to mineralization in gold. (For interpretation of the references to colour in this figure legend, the reader is referred to the Web version of this article.)

Acknowledgements

This research paper is a component of Dr. Yaya Fodoue and Safianou Ousmanou research work. The authors address their special thanks to the authorities and population of Bibemi area for their collaboration, and hospitality. Thanks also to anonymous reviewers and editors for their continuous quick assessment.

References

[1] M. Abdelkareem, F. El-Baz, Characterizing hydrothermal alteration zones in Hamama area in the central Eastern Desert of Egypt by remotely sensed data, Geocarto Int. 33 (2018) 1307–1325.
[2] M. Abdelkareem, N. Al-Arifi, Synergy of remote sensing data for exploring hydrothermal mineral resources using GIS-based fuzzy logic approach, Remote Sens 13 (2021) 4492.
[3] A. Abdel nasser, M. Kumral, B. Zoheir, M. Karaman, REE geochemical characteristics and satellite-based mapping of hydrothermal alteration in Atud gold deposit. Egypt, J. Afr. Earth Sci. 145 (2018) 317–330.
[4] M.J. Abrams, D. Brown, L. Lepley, R. Sadowski, Remote sensing for porphyry copper deposits in southern Arizona, Econ. Geol. 78 (1983) 591–604.
[5] M. Abrams, The advanced spaceborne thermal emission and reflection radiometer (ASTER): data products for the high spatial resolution imager on NASA's terra platform, Int. J. Rem. Sens. 21 (5) (2000) 847–859.

[6] S.S. Alarifi, M. Abdelkareem, F. Abdalla, I.S. Abdelsadek, H. Gahlan, A.M. Al-Saleh, M. Alotaibi, Fusion of multispectral remote-sensing data through GIS-based overlay method for revealing potential areas of hydrothermal mineral resources, Minerals 12 (2022) 1577.
[7] R. Amer, A. El Mezayen, M. Hasanein, ASTER spectral analysis for alteration minerals associated with gold mineralization, Ore Geol. Rev. 75 (2016) 239–251.
[8] L.S. Bernstein, X. Jin, B. Gregor, S. Adler-Golden, Quick atmospheric correction code: algorithm description and recent upgrades, Optical Engineering 51, 11: 111719-1 to (2012) 111719, 11.
[9] S.M. Bolouki, H.R. Ramazi, A. Maghsoudi, A. Beiranvand Pour, G. Sohrabi, A remote sensing-based application of bayesian networks for epithermal gold potential mapping in ahar-arasbaran area. NW Iran, Rem. Sens. 12 (2020) 105.
[10] M. Bouyo Houketchang, S.F. Toteu, E. Deloule, J. Penaye, W.R. Van Schmus, U–Pb and Sm–Nd dating of high-pressure granulites from Tcholliré and Banyo regions: evidence for a Pan-African granulite facies metamorphism in northcentral Cameroon, J. Afr. Earth Sci. 54 (2009) 144–154.
[11] C. Braitenberg, P. Mariani, J. Ebbing, P.M.M. Sprlak, The enigmatic Chad lineament revisited with global gravity and gravity-gradient fields, Geol. Soc. Lond. Spec. Publ. 357 (2011) 329–341.
[12] L.D. Campos, S.M. de Souza, D.A. de Sordi, F.M. Tavares, E.L. Klein, E.C.D.S. Lopes, Predictive mapping of prospectivity in the Gurupi orogenic gold belt, north–northeast Brazil: an example of district scale mineral system approach to exploration targeting, Nat. Resour. Res. 26 (2017) 509–534.
[13] A. Crosta, J. Moore, Enhancement of Landsat thematic mapper imagery for residual soil mapping in SW Minais Gerais State, Brazil: a prospecting case history in greenstone belt terrain, International proceedings of the Seventh Erim Thematic Conference on Remote Sens Expl Geol (1989) 1173–1187.
[14] A.P. Crosta, C.R. De Souza Filho, F. Azevedo, C. Brodie, Targeting key alteration minerals in epithermal deposits in Patagonia, Argentina, using ASTER imagery and principal component analysis, Int. J. Rem. Sens. 24 (2003) 4233–4240.
[15] D. Dawaï, J.L. Bouchez, J.L. Paquette, R. Tchameni, The Pan-African quartzsyenite of Guider (north-Cameroon): magnetic fabric and U-Pb dating of a lateorogenic emplacement, Precambrian Res. 236 (2013) 132–144.
[16] D.F. Ducart, A.P. Crosta, C.R.S. Filio, Alteration mineralogy at the Cerro La Mina epithermal prospect, Patagonia, Argentina: field mapping, short-wave infrared spectroscopy, and ASTER images, Econ. Geol. 101 (2006) 981–996.
[17] S.J. Fraser, Discrimination and identification of ferric oxides using satellite Thematic Mapper data: a Newman case study, Int. J. Rem. Sens. 12 (1991) 635–641.
[18] S. Gabr, A. Ghulam, T. Kusky, Detecting areas of high-potential gold mineralization using ASTER data, Ore Geol. Rev. 38 (1) (2010) 59–69.
[19] R.P. Gupta, Remote Sensing Geology, Springer, 2003, https://doi.org/10.1007/978-3-662-05283-9.
[20] R.P. Gupta, R.K. Tiwari, V. Saini, N. Srivastava, A simplified approach for interpreting principal component images, Adv. Rem. Sens. 2 (2013) 111–119.
[21] R.P. Gupta, Remote Sensing Geology, 3rd Edn, Springer, Berlin, Germany, 2017, pp. 180–787, 190, 235-240, and 332-336.
[22] M.M. Ishagh, A.B. Pour, H. Benali, A.M. Idriss, S.A.S. Reyoug, A.M. Muslim, M.S. Hossain, Lithological and alteration mapping using Landsat 8 and ASTER satellite data in the Reguibat Shield (West African Craton), North of Mauritania: implications for uranium exploration, Arab J Geosci 14 (2021) 2576.
[23] H. Kaufmann, Mineral exploration along the Aqaba-Levant Structure by use of TM data. Concepts, processing and results, Int. J. Remote. Sens. 9 (1988) 1639–1658.
[24] Y.H. Kim, K.U. Choe, R.K. Ri, Application of fuzzy logic and geometric average: a Cu sulfide deposits potential mapping case study from Kapsan Basin, DPR Korea, Ore Geol. Rev. 107 (2019) 239–247.
[25] F.A. Kruse, A.B. Lefkoff, J.B. Boardman, K.B. Heidebrecht, A.T. Shapiro, P.J. Barloon, A.F. Goetz, The spectral image processing system (SIPS) – interactive visualization and analysis of imaging spectrometer data, Remote Sens. Env. 44 (1993) 145–163.
[26] J.P. Liegeois, G.M. Abdelsalam, N. Ennih, A. Ouabadi, Metacraton: nature, genesis and behavior, Gondwana Res. 23 (2013) 220–237.
[27] L. Liu, D.F. Zhuang, J. Zhou, D.S. Qiu, Alteration mineral mapping using masking and Crosta technique for mineral exploration in mid-vegetated areas: a case study in Areletuobie, Xinjiang (China), Int. J. Rem. Sens. 32 (2011) 1931–1944.
[28] W. Loughlin, Principal component analysis for alteration mapping, Photogramm. Eng. Rem. Sens. 57 (9) (1991) 1163–1169.
[29] P. Louis, Contribution géophysique à la connaissance géologique du bassin du Lac Tchad, Memoires ORSTOM, Paris, 1970, p. 308.
[30] T. Mamadou, D.T.W. Jonas, P.N. Cyrille, T. Senem, P. Amin Beiranvand, M.M. Aidy, Lithological and alteration mineral mapping for alluvial gold exploration in the south east of Birao area, Central African Republic using Landsat-8 Operational Land Imager (OLI) data, J. Afr. Earth Sci. 170 (2020) 103–933.
[31] J.C. Mars, L.C. Rowan, Regional mapping of phyllic- and argillic-altered rocks in the Zagros magmatic arc, Iran, using Advanced Space borne Thermal Emission and Reflection Radiometer (ASTER) data and logical operator algorithms, Geosphere 2 (2006) 161–186.
[32] E. Nomo Negue, R. Tchameni, O. Vanderhaeghe, F. Sun, P. Barbey, L. Tekoum, P.M. Fosso Tchunte, A. Eglinger, N.A. Saha Fouotsa, Structure and LA-ICP-MS zircon U-Pb dating of syn-tectonic plutons emplaced in the Pan-African Banyo-Tcholliré e shear zone (central north Cameroon), J. Afr. Earth Sci. 131 (2017) 251–271.
[33] V. Novák, I. Perfilieva, J. Močkoř, Mathematical Principles of Fuzzy Logic, Kluwer 928 Academic, Dordrecht, 1999, 978-0-7923-8595-0.
[34] I.D. Novak, N. Soulakellis, Identifying geomorphic features using LANDSAT-5/TM data processing techniques on lesvos, Greece, Geomorphology 34 (2000) 101–109.
[35] S. Ousmanou, E.M. Fozing, M. Kwékam, F. Yaya, D.A.J. Leprince, Application of remote sensing techniques in lithological and mineral exploration: discrimination of granitoids bearing iron and corundum deposits in southeastern Banyo, Adamawa region- Cameroon, Earth Sci Inform 1–27 (2023), https://doi.org/10.1007/s12145-023-00937-5.
[36] J. Penaye, A. Kröner, S.F. Toteu, W.R. Van Schmus, J.C. Doumnang, Evolution of the Mayo-Kebbi region as revealed by zircon dating: an early (ca. 740 Ma) PanAfrican magmatic arc in southwestern Chad, J. Afr. Earth Sci. 44 (2006) 530–542.
[37] B.A. Pour, M. Hashim, J. van Genderen, Detection of hydrothermal alteration zones in a tropical region using satellite remote sensing data: bau gold field, Sarawak, Malaysia, Ore Geol. Rev. 54 (2013) 181–196.
[38] B.A. Pour, M. Hashim, M. Marghany, Exploration of gold mineralization in a tropical region using Earth Observing-1 (EO1) and JERS-1 SAR data: a case study from Bau gold field, Sarawak, Malaysia, Arbian J. Geosci. 7 (6) (2014) 2393–2406.
[39] B.A. Pour, M. Hashim, Hydrothermal alteration mapping from Landsat-8 data, SarCheshmeh copper mining district, south-eastern Islamic Republic of Iran, J. Taibah Univ. Sci. 9 (2015) 155–166.
[40] A.B. Pour, M. Hashim, Y. Park, J.K. Hong, Mapping alteration mineral zones and lithological units in Antarctic regions using spectral bands of ASTER remote sensing data, Geocarto Int. 32 (12) (2018) 1281–1306.
[41] A.B. Pour, Y. Park, T.S. Park, J.K. Hong, M. Hashim, J. Woo, I. Ayoobi, Evaluation of ICA and CEM algorithms with Landsat-8/ASTER data for geological mapping in inaccessible regions, Geocarto Int. (2018), https://doi.org/10.1080/10106049.2018.1434684.
[42] A.B. Pour, Y. Park, T.S. Park, J.K. Hong, M. Hashim, J. Woo, I. Ayoobi, Regional geology mapping using satellite-based remote sensing approach in Northern Victoria Land, Antarctica, Polar Sci 16 (2018) 23–46.
[43] A.B. Pour, T.S. Park, Y. Park, J.K. Hong, B. Zoheir, B. Pradhan, I. Ayoobi, M. Hashim, Application of multi-sensor satellite data for exploration of Zn-Pb sulphide mineralization in the Franklinian Basin. North Greenland, Rem. Sens. 10 (2018) 1186, https://doi.org/10.3390/rs10081186.
[44] A.B. Pour, M. Hashim, J.K. Hong, Y. Park, Lithological and alteration mineral mapping in poorly exposed lithologies using Landsat-8 and ASTER satellite data: north-eastern Graham Land, Antarctic Peninsula, Ore Geol. Rev. 108 (2019) 112–133.
[45] A.B. Pour, Y. Park, L. Crispini, A. Läufer, J. Kuk Hong, T.Y.S. Park, B. Zoheir, B. Pradhan, A.M. Muslim, M.S. Hossain, O. Rahmani, Mapping listvenite occurrences in the damage zones of northern victoria land, Antarctica using ASTER satellite remote sensing data, Rem. Sens. 11 (2019) 1408, https://doi.org/10.3390/rs11121408.
[46] A.B. Pour, T.Y. Park, Y. Park, J.K. Hong, A.M. Muslim, A. Läufer, L. Crispini, B. Pradhan, B. Zoheir, O. Rahmani, M. Hashim, M.S. Hossain, Landsat-8, advanced space borne thermal emission and reflection radiometer, and WorldView-3 multispectral satellite imagery for prospecting copper-gold mineralization in the northnorth-eastern inglefield mobile belt (IMB). Northwest Greenland, Remote Sens. 2019 (11) (2019) 2430, https://doi.org/10.3390/rs11202430.
[47] H. Ranjbar, M. Honarmandb, Z. Moezifar, Application of the Crosta technique for porphyry copper alteration mapping, using ETM+ data in the southern part of the Iranian volcanic sedimentary belt, J. Asian Earth Sci. 24 (2004) 237–243.
[48] F. Sabins, Remote Sensing Principles and Interpretation, third ed., W.H. Freeman Company, New York, NY, USA, 1997, p. 494.

[49] F.F. Sabins, Remote sensing for mineral exploration, Ore Geol. Rev. 14 (1999) 157–183.
[50] O. Safianou, E.M. Fozing, K.J. Tcheumenack, M.L. Achu, T.A.B. Kamgang, S. Aman, M. Rachid, M. Kwékam, Mapping and discrimination the mineralization potential in the granitoids from Banyo area (Adamawa, Cameroon), using Landsat 9 OLI, ASTER images and field observation, GeoGeo 100239 (2023), https://doi.org/10.1016/j.geogeo.2023.100239.
[51] S.M. Salem, M. El Sharkawi, Z. El-Alfy, N.M. Soliman, S.E. Ahmed, Exploration of gold occurrences in alteration zones at Dungash district, Southeastern Desert of Egypt using ASTER data and geochemical analyses, J. Afr. Earth Sc. 117 (2016) 389–400.
[52] P. Schwoerer, Carte géologique de reconnaissance du Cameroun au 1/500000ème. Feuille NC 33 SO 0 53 Gaoua-Est avec notice explicative, in: Direction des Mines et de la Géologie du Cameroun. Imprimerie Nationale, Publication de la, Yaoundé Cameroun, 1962.
[53] A. Sheikhrahimi, B.A. Pour, B. Pradhan, B. Zoheir, Mapping hydrothermal alteration zones and lineaments associated with orogenic gold mineralization using ASTER remote sensing data: a case study from the Sanandaj-Sirjan Zone. Iran, Adv. Space Res. 63 (2019) 3315–3332.
[54] K. Shi, Z. Chang, Z. Chen, J. Wu, B. Yu, Identifying and evaluating poverty using multisource remote sensing and point of interest (POI) data: a case study of Chongqing, China, J. Clean. Prod. 255 (2020), 120245.
[55] J.D. Takodjou Wambo, S. Ganno, Y.S. Djonthu Lahe, G.D. Kouankap Nono, D.H. Fossi, M.S. Tchouatcha, J.P. Nzenti, Geostatistical and GIS analysis of the spatial variability of alluvial gold content in Ngoura-Colomines area, Eastern Cameroon: implications for the exploration of primary gold deposit, J. Afr. Earth Sci. 142 (2018) 138–157.
[56] J.D. Takodjou Wambo, A.B. Pour, S. Ganno, P.D. Asimow, B. Zoheir, R. dos Reis Salles, J. Paul Nzenti, B. Pradhan, A.M. Muslim, Identifying high potential zones of gold mineralization in a sub-tropical region using Landsat-8 and ASTER remote sensing data: a case study of the Ngoura-Colomines goldfield, Eastern Cameroon, Ore Geol. Rev. 122 (2020), 103530.
[57] F.J. Testa, C. Villanueva, D.R. Cooke, L. Zhang, Lithological and hydrothermal alteration mapping of epithermal, porphyry and tourmaline breccia districts in the Argentine andes using ASTER imagery, Remote. Sens. 10 (2018) 203.
[58] S.F. Toteu, W.R. Van Schmus, J. Penaye, A. Michard, New U–Pb and Sm–Nd data from north-central Cameroon and its bearing on pre-Pan-African history of central Africa, Precambrian Res. 108 (2001) 45–73.
[59] S.F. Toteu, J. Penaye, D.Y. Poudjom, Geodynamic evolution of the Pan-African belt of Central Africa with special reference to Cameroon, Can. J. Earth Sci. 41 (2004) 73–85.
[60] S.F. Toteu, J. Penaye, E. Deloule, W.R. Van Schmus, R. Tchameni, Diachronous evolution of volcano-sedimentary basins north of the Congo craton: insights from U–Pb ion microprobe dating of zircons from the Poli, Lom and Yaounde Series (Cameroon), J. Afr. Earth Sci. 44 (2006) 428–442.
[61] W.R. Van Schmus, E.P. Oliveira, A.F. da Silva Filho, S.F. Toteu, J. Penaye, I.P. Guimaraes, Proterozoïc links between the borborema province, NE ~ Brazil, and the central african fold belt, Geol. Soc. Lond. Spec. Publ. 294 (2008) 69–99.
[62] X. Zhang, M. Pazner, N. Duke, Lithologic and mineral information extraction for gold exploration using ASTER data in the south Chocolate Mountains (California), ISPRS J. Photogramm. Remote. Sens. 62 (2007) 271–282.
[63] N. Zhang, K. Zhou, X. Du, Application of fuzzy logic and fuzzy AHP to mineral prospectivity mapping of porphyry and hydrothermal vein copper deposits in the Dananhu Tousuquan island arc, Xinjiang, NW China, J. Afr. Earth Sci. 128 (2017) 84–96.
[64] B.A. Zoheir, P. Weihed, Greenstone-hosted lode-gold mineralization at dungash mine, Eastern Desert, Egypt, J. Afr. Earth Sci. 99 (2014) 165–187.
[65] B. Zoheir, A. Emam, M. El-Amawy, T. Abu-Alam, Auriferous shear zones in the central Allaqi-Heiani belt: orogenic gold in post-accretionary structures, SE Egypt, J. African Earth Sci. 146 (2017) 118–131, https://doi.org/10.1016/j.jafrearsci.2017.10.017.
[66] B. Zoheir, A. Emam, M. Abdel-Wahed, N. Soliman, Multispectral and radar data for the setting of gold mineralization in the south Eastern Desert, Egypt, Rem. Sens. 11 (2019) 1450, https://doi.org/10.3390/rs11121450.